Final Report

# Remote Infrared Thermography for In-Flight Flow Diagnostics

by

H.J. Shiu and C.P. van Dam
Department of Mechanical and Aeronautical Engineering
University of California, Davis
One Shields Avenue
Davis, CA 95616

to

D.W. Banks
Mail Stop D-2027
NASA Dryden Flight Research Center
Edwards, CA 93523

NASA NCC4-114

February 1999

## Nomenclature

| | |
|---|---|
| $\alpha$ | angle of attack |
| c | chord |
| $c_f$ | coefficient of skin friction (based on freestream properties) |
| $\varepsilon$ | emissivity |
| k | thermal conductivity |
| $\lambda_p$ | peak wavelength |
| $\mu$ | absolute viscosity |
| $q''$ | rate of heat transfer per unit area |
| $\rho$ | density |
| $\rho_\infty$ | freestream density |
| $\sigma$ | Stefan-Boltzmann constant |
| T | temperature |
| $T_{t_\infty}$ | stagnation (total) temperature of freestream |
| $T_W$ | wall (surface) temperature |
| $U_\infty$ | freestream velocity |
| $(x/c)_{trans}$ | location of laminar to turbulent transition, normalized by chord |

**Abstract**
The feasibility of remote in-flight boundary layer visualization via infrared in incompressible flow was established in earlier flight experiments. The past year's efforts focused on refining and determining the extent and accuracy of this technique of remote in-flight flow visualization via infrared. Investigations were made into flow separation visualization, visualization at transonic conditions, shock visualization, post-processing to mitigate banding noise in the NITE Hawk's thermograms, and a numeric model to predict surface temperature distributions. Although further flight tests are recommended, this technique continues to be promising.

## I. Introduction

In recent years, interest has continued in the development of low-drag airplanes with extended runs of laminar flow. This interest has resulted in demand for wind tunnel and flight experiments to investigate the extent of laminar flow on wings and bodies and the sensitivity of the laminar flow to manufacturing tolerances and surface contamination. Furthermore, a greater awareness has recently developed for the effects of laminar flow on the high-angle-of-attack characteristics of maneuverable military aircraft and the high-lift characteristics of transport aircraft. Flow separation at these conditions is related to the extent of laminar flow and, thus, to the phenomenon of laminar-turbulent transition. To better predict the aerodynamic forces generated by aircraft at high-angle-of-attack and/or high-lift conditions, an improved understanding of the transition phenomena at full-scale flight conditions is required.

A large number of techniques is available to study boundary-layer transition on aircraft surfaces including sublimating chemicals[1], oil flow[2], liquid crystals[3], luminescent temperature-sensitive paints[4], surface oil film interferometry[5], hot-film anemometry[3,6,7], thermocouples[3], microphones[7], total pressure (Preston) tubes[8], infrared thermography[2,3,6], etc.

Several of these transition detection techniques are intrusive; that is, they affect the development of the laminar boundary layer and, thus, transition. Devices such as thin hot films, thermocouples, and microphones provide excellent quantitative information on transition. However, the information is strictly local and many tightly spaced hot films, thermocouples, or microphones are required to obtain sufficient global information. Techniques such as sublimating chemicals and oil flow remain very popular for transition measurement in ground-based facilities. Unfortunately, only one condition per surface application can be tested and this limitation makes these techniques less desirable for flight experimentation. Recently, techniques based on surface application of liquid crystals and luminescent temperature-sensitive paints have received more attention. These techniques require more-or-less permanent surface treatment – something that may be less than desirable – as well as a significant amount of preparation and calibration time. Also, some of these materials are considered to be hazardous and thus require special preflight and postflight procedures for application and removal. As a result of these insufficiencies and drawbacks, infrared thermography is often the preferred technique to study transition because it (1) is nonintrusive, (2) provides global information, (3) is reversible, and (4) requires no or minimal treatment of the surface in the subject area.

Infrared imaging systems have been successfully installed within a subject aircraft to visualize flow on surfaces of that aircraft[2,6,9]. Such an installation limits infrared studies to only that one aircraft. Furthermore, use of an infrared imager within a subject aircraft

requires the expensive installation of a viewing window made of special materials such as germanium, zinc sulfide, or zinc selenide. Difficulties may also arise in obtaining an adequate field of view. Although this is less of a problem for larger transport aircraft with windows a significant distance above the wing[6], it is significant for smaller light aircraft[2,9] and military aircraft. Remote infrared imaging can address these issues as demonstrated by the Infra-Red Imagery of the Shuttle (IRIS) experiment conducted during the initial shuttle flights[10,11,12]. By placing the infrared imaging system on a separate aircraft and flying this aircraft in close formation with a subject aircraft, thermograms can be captured of the subject's surface over a wide field of view with little or no modification required on the subject. In the present study, NASA Dryden Flight Research Center's F/A-18 #846 with the NITE Hawk FLIR was employed as the imaging aircraft.

In the following section, the principles of remote in-flight infrared imaging and flight experiment specifics are provided. In Section III, earlier studies of this technique are briefly reviewed and then the following research investigations of the past year are detailed:

a. visualization of flow separation
b. flow visualization at transonic conditions
c. visualization of shocks
d. removal of horizontal banding
e. surface temperature prediction model

## II. Theory & Methods

Visualization via infrared thermography works by detecting the boundary layer state dependent temperature differences between the subject surface and the flow. Infrared imaging systems detect thermal emissions radiated by a body and record them as intensity values in an image. Given the emissivity, a surface property discussed further in Section IIIe, the temperature distribution of the subjects in the image can be deduced.

On an aircraft in flight, several sources of heat transfer contribute to surface temperature changes including: convection, recovery factor in compressible flow, radiation from the surface to the environment, radiation from the sun and the atmosphere to the surface, conduction within the surface, conduction to/from internal structure or fuel beneath the surface, and changes in altitude.

### IIa. At low Mach numbers ($M_\infty << 1$)

At low Mach numbers, transition can be visualized via infrared because the convective heat transfer is closely related to skin friction which, in turn, is closely related to the boundary layer state. Heat transfer and skin friction are related as follows:

$$q'' = \frac{c_f}{2} \rho_\infty U_\infty (T_W - T_{t_\infty}) \frac{k}{\mu} \qquad [1]$$

Skin friction, $c_f$, and therefore heat transfer is higher in the turbulent boundary layer than in the laminar boundary layer.

A steady state temperature difference between the surface and the flow can be created by cooling or heating the flow or by cooling or heating the surface. In ground-based facilities, the flow temperature often can be regulated; however, except for indirect control via altitude changes, this is unavailable in flight experiments. Several techniques are available to heat or cool the surface. Passively, solar radiation and atmospheric emissions naturally

contribute to surface heating and cooling. Actively, Horstmann et al[13] utilized a heating sheet to raise the surface temperature. Unfortunately, this is only practical when a glove is used to raise the test surface and provide space for surface heaters.

If $T_W > T_{t_\infty}$, the laminar surface will be slightly warmer than the turbulent surface and slightly cooler if $T_W < T_{t_\infty}$. This surface temperature difference is especially noticeable at transition; it is this difference that is detected by the infrared imager.

### IIb. At higher Mach numbers

In addition to convective heat transfer, at higher Mach numbers, a temperature difference is created by the reduced recovery factor in the boundary layer. In compressible flow, the recovery factor is less than unity, causing the wall temperature to be less than the total temperature of the undisturbed flow ($T_W < T_{t_\infty}$). The recovery factor is dependent on the boundary layer state with laminar flow having a slightly lower value than turbulent flow. The laminar surface is therefore slightly cooler than the turbulent surface.

### IIc. Flight experiment procedure

As detailed in earlier documents[14,15], the imaging aircraft flies in formation with a subject aircraft and captures thermograms of the subject. The block diagram in Figure 1 outlines the in-flight and post-flight procedures of remote in-flight transition visualization with infrared thermography.

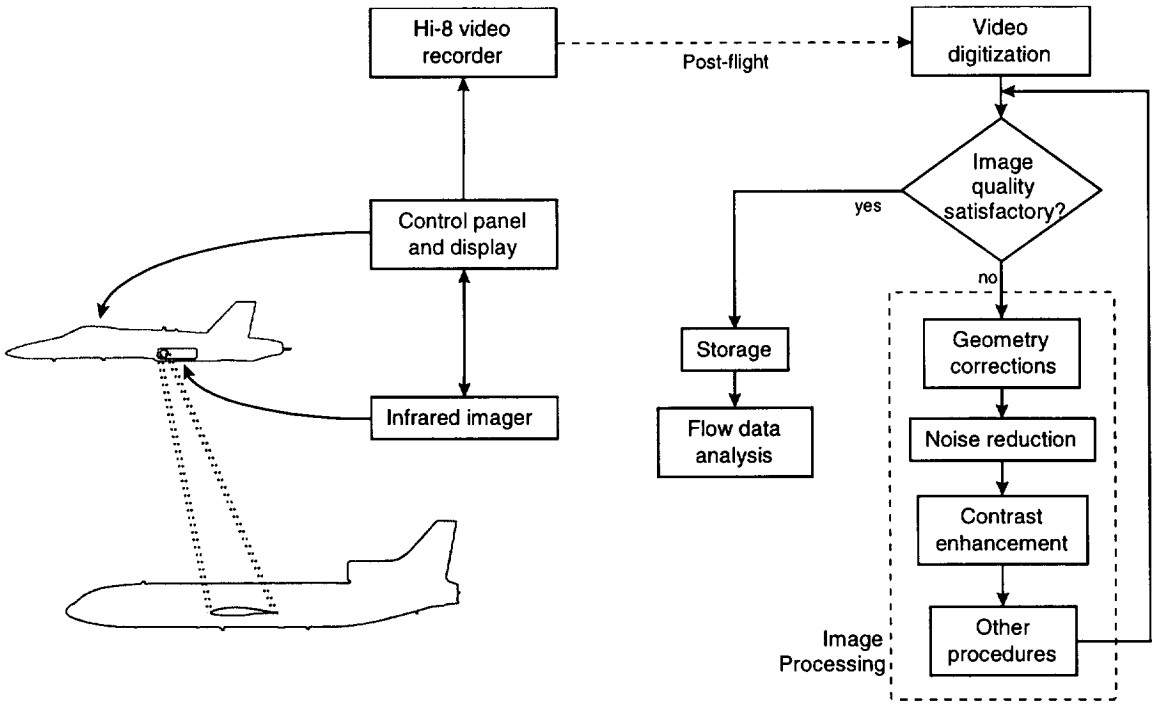


**Figure 1.** The principle steps of flow visualization via remote in-flight infrared thermography.

In the flight experiments to date, NASA Dryden's F/A-18 #846 with the NITE Hawk FLIR was employed as the imaging aircraft. Subject surfaces on the subject aircraft were covered with a self-adhesive, thin, insulative, black film to reduce glare, mitigate flattening of

temperature gradients by lateral heat conduction within the aircraft skin, and improve emissivity. Digital post-processing techniques such as image averaging and histogram stretching were used to enhance the captured thermograms. Details are available in earlier documents.[14,15]

## IId. NITE Hawk infrared imaging system

The AN/AAS-38 NITE Hawk FLIR has been the centerpiece of the flight experiments in this investigation. Designed as a targeting system, the NITE Hawk has been successfully used to record thermograms for flow visualization. The NITE Hawk system installed in NASA Dryden's F/A-18 #846 includes a visible spectrum camera collocated with the infrared imager in the pod. Specifications of the NITE Hawk are provided below in Figure 2.

- spectral sensitivity: 8 to 12 μm
  -32°C to 89°C
- thermal sensitivity: < 0.1°F
- image field: 3° × 3°
  12° × 12°
- field of regard: +30° to -165° pitch
  ±540° roll
- resolution: 875 lines
- scanned 128×2 detector array
- automatic tracking available
- visible spectrum camera collocated with infrared imager
- output to standard Hi-8 video

**Figure 2.** Specifications and close-up photograph[16] of the AN/AAS-38 NITE Hawk FLIR.

## III. Research progress in 1998

The feasibility of remote in-flight boundary layer visualization via infrared was first verified at subsonic conditions with the T-34C as the subject aircraft.[14] As shown in Figure 3, the captured thermograms showed transition at approximately 21% of chord, which correlates well with numeric simulations.

The thermograms recorded by F/A-18 #846's NITE Hawk all exhibited horizontal banding which limited analysis of the captured images. However, large temperature differences such as those associated with transition remain visible.

Research efforts since the initial T-34C flight experiments are detailed below.

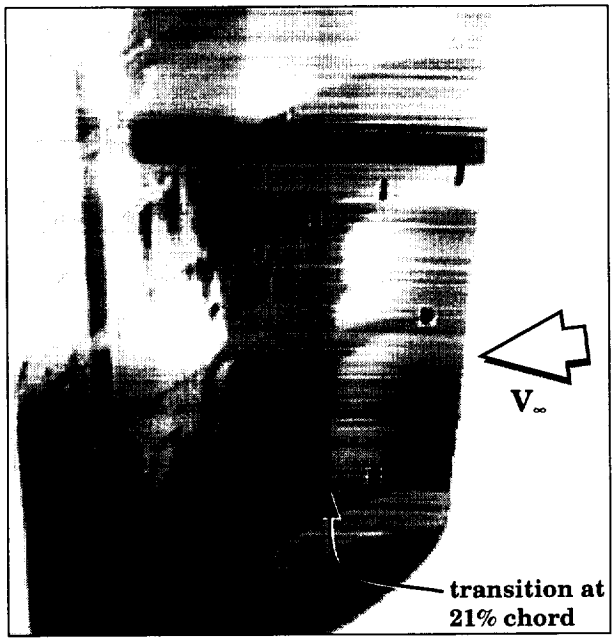


**Figure 3.** Thermogram of the T-34C at 10,000 feet, approximately 160 KCAS. The upper surface of the outboard region of the starboard wing is shown. Transition is visible at approximately 21% of chord.

### IIIa. Visualization of flow separation

An in-flight experiment was proposed to investigate the feasibility of turbulent separation visualization via infrared imaging. When the Learjet 24 became available as a subject aircraft, this experiment was deferred.

Installation of a tab on the wing surface was proposed to induce separation on the wing of a T-34C. Numerical simulations were performed to verify the effectiveness of a tab in generating flow separation. INS2D[17,18], an incompressible two-dimensional Navier-Stokes code, was used with the following conditions:

airfoil: NACA 23012
altitude: 10,000 feet
speed: 165 KCAS
$\alpha$: 1°
chord: 5.1 feet

The chord corresponds to a wing station just inboard of the ailerons where separation would not affect the effectiveness of control surfaces and contamination from the fuselage and engine exhaust is minimal. 165 KCAS is approximately the T-34's maximum airspeed in level flight; at lower speeds, the relatively high speed F/A-18 imaging aircraft has difficulty maintaining formation flight. The tabs were located in turbulent flow at 30% of chord with heights of 0.5%, 1.0%, 1.5%, 2.0%, 3.0% and 4.0% of chord.

The results of the numerical simulations for a 0.5% of chord tab are shown in Figures 4a through 4c. The simulations show that flow aft of the tab is not completely detached. Instead, as seen in Figure 4b, a stable "bubble" of recirculating flow forms immediately behind the tab and the flow reattaches further downstream. The size of the bubble increases with the height of the tab. With a 0.5% of chord tab, the bubble extends to

approximately 40% of chord; with tabs taller than 1.5% of chord, the bubble extends almost to the trailing edge.

From inspection of the skin friction values, as shown for the 0.5% case in Figure 4c, infrared imaging is unlikely to visualize this phenomenon well. Note that only the magnitude of skin friction is important; convective heat transfer occurs regardless of the flow direction. Because the magnitudes of skin friction inside and outside the bubble are approximately the same, only the edges of the bubble may show a detectable temperature difference. However, the temperature gradients due to the downward spikes in skin friction magnitude at the edges are likely to be lost because of heat conduction within the skin. The effects of conduction within the skin are further discussed below in Section IIIe, *Wing surface temperature model.*

In the numerical simulations, the tabs do not produce the desired flow phenomenon. The bubbles created by the tabs are difficult to visualize with temperature dependent methods such as infrared imaging. It may be possible to induce more "traditional" separation with completely detached flow by increasing angle of attack or increasing surface roughness downstream of the tab. Increasing angle of attack would further slow the T-34C in level flight, further complicating imaging with the relatively high speed F/A-18.

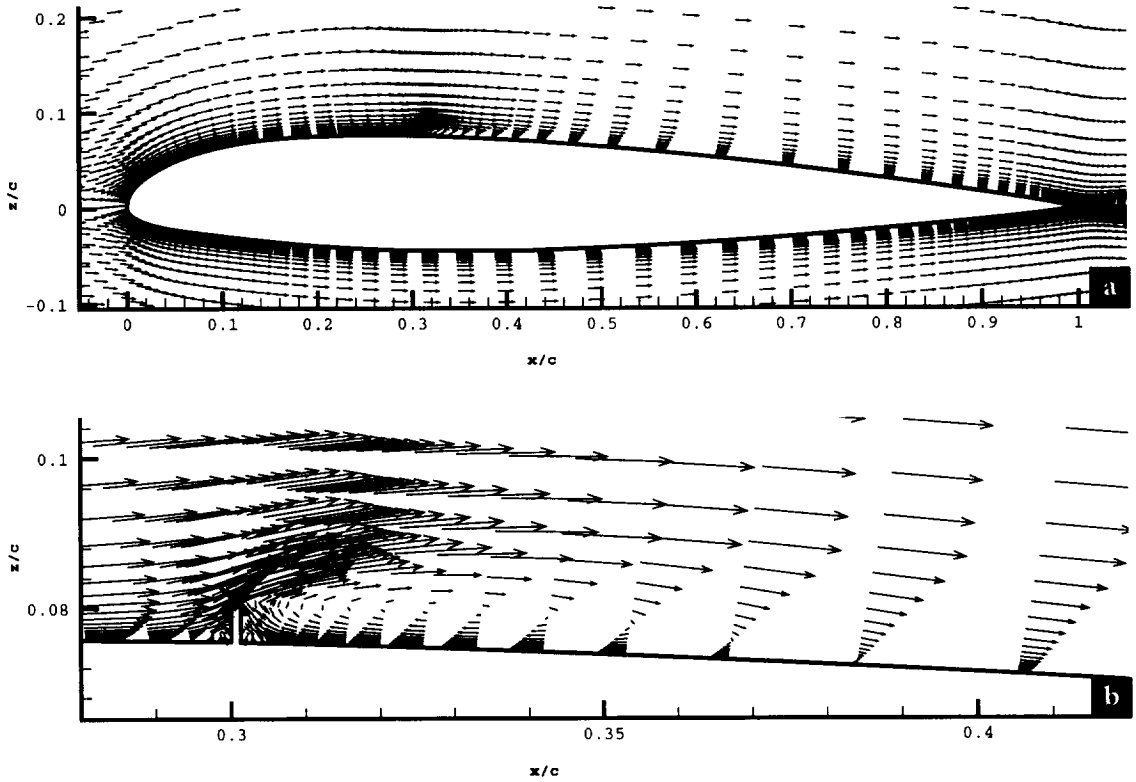


**Figures 4a and 4b.** Flow field about the T-34C wing with a 0.5% of chord tab at 30% of chord.

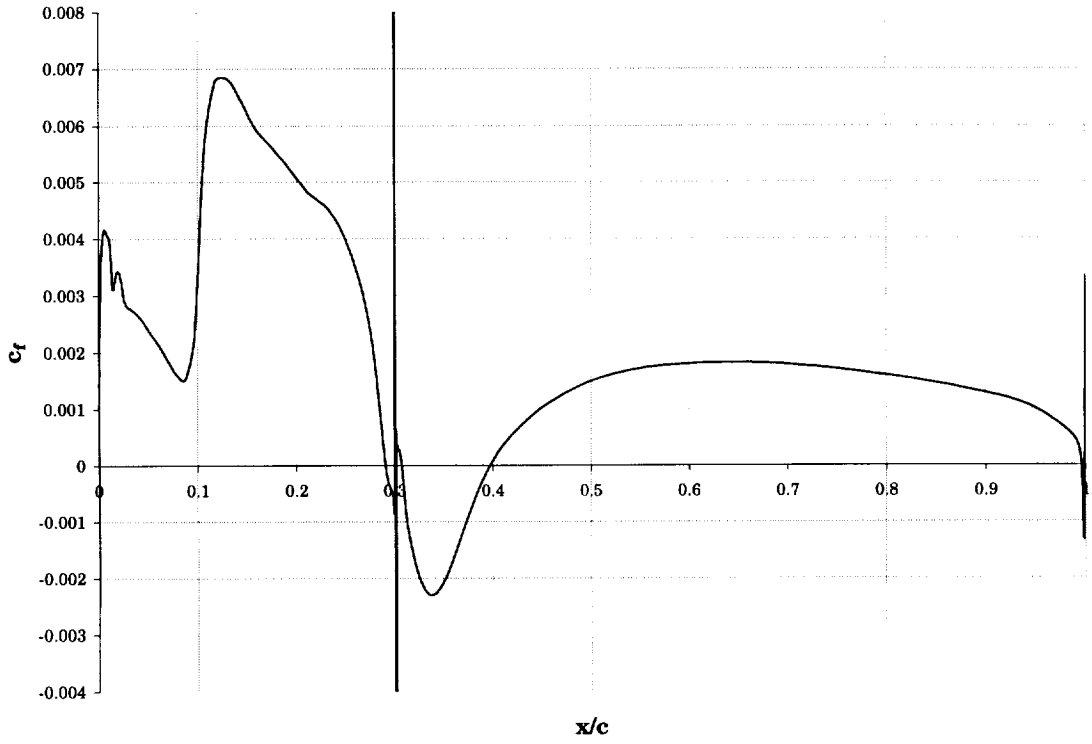


**Figure 4c.** Skin friction distribution on the upper surface of the T-34C wing with a 0.5% of chord tab at 30% of chord.

## IIIb. Flow visualization at transonic conditions

With the availability of the Learjet 24 as a subject aircraft, the feasibility of in-flight infrared transition visualization at transonic conditions was investigated. In the transonic regime, the effect of the dissimilar recovery factor in the laminar and turbulent boundary layers cannot be ignored as in incompressible flow.

Two flight tests were performed at altitudes up to 40,000 feet and Mach numbers up to 0.79. The primary subject area, shown in Figures 5a and 5b, was on the upper surface of the starboard wing, just outboard of the boundary layer fence. As with earlier experiments with the T-34C, the subject area was covered with self-adhesive, black, insulative film. For comparison with the captured thermograms, numerical simulations of the Learjet's airfoil, a modified NACA 64A109, were performed with MSES[19], a two-dimensional Euler/boundary layer code.

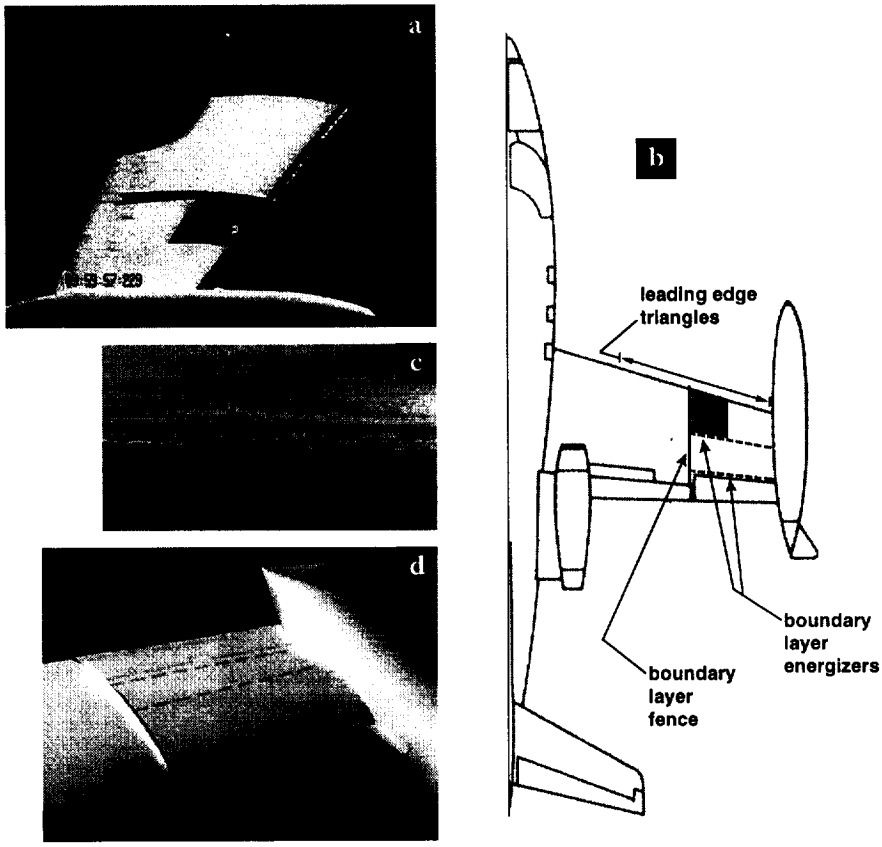


**Figure 5a.** The subject area on the Learjet 24. **5b.** A planview[20] of the Learjet 24 with the Softflite kit. The subject area, leading edge triangles, boundary layer energizers (BLEs), and boundary layer fence are indicated. **5c.** The Softflite kit's leading edge triangles on a Learjet.[21] **5d.** The Softflite kit's boundary layer energizers (BLEs) on a Learjet.[22]

At 40,000 feet, Mach 0.77, numerical simulations predict transition at 53% of chord on a clean lifting surface with a small sweep angle. Figure 6 shows the thermogram of the subject area on the Learjet 24 at 40,000 feet, Mach 0.77.

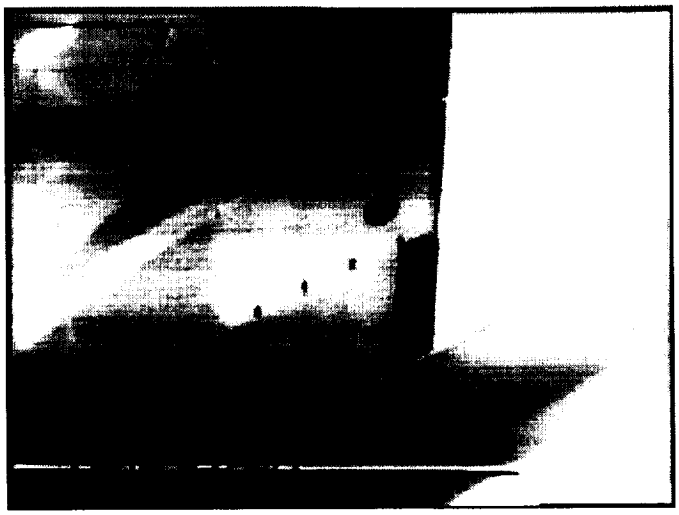

**Figure 6.** Thermogram of the Learjet 24 at 40,000 feet, Mach 0.77.

The leading edge is right of the center. The reflective chrome surface of the leading edge has a low emissivity and appears black. The tip tank is at the bottom of the image. The subject area, with black, insulative film applied, appears as a lighter region with distinct edges. A circular trip made with reflective aluminum tape is visible on the subject area near the leading edge. Boundary layer energizers, the boundary layer fence, and a reflection of the starboard engine nacelle are also visible. No intensity changes are visible indicating transition or a turbulent wedge off the trip.

The lack of a turbulent wedge originating at the trip suggests that flow over the entire subject area may be turbulent. The Softflite kit installed on the Learjet 24 for improvement of stall handling characteristics includes a row of short triangles along the leading edge[23], shown in Figures 5b and 5c. These leading edge triangles likely contaminate the attachment line boundary layer, causing turbulent flow over the entire surface aft of them. Figure 7 shows an inboard section of the starboard wing. The Softflite kit's leading edge triangles are not installed this far inboard. This thermogram was taken at 40,000 feet at approximately Mach 0.79.

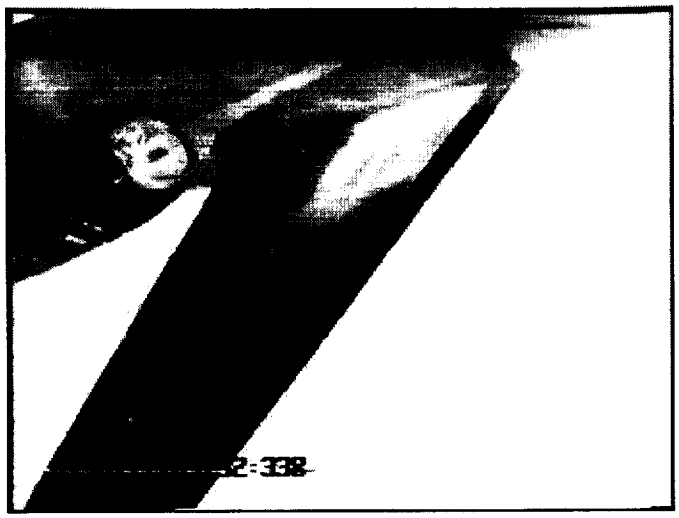

**Figure 7.** Thermogram of the Learjet 24 at 40,000 feet, Mach 0.79. The inboard region of the starboard wing is shown.

A light intensity, warmer region exists up to approximately half-chord. Without leading edge triangles to prematurely trip the flow, this may be a laminar flow region. However, the possibility of flow interference with the fuselage and the lack of surface treatment with the black, insulative film make analysis of this wing section indeterminate.

Pending safety considerations, more conclusive results may be obtained by flight testing again at the same conditions with surface treatment applied to the inboard sections of the wing.

Unexpected flow phenomena were visualized aft of the subject area. Figure 8 shows the subject area on the Learjet at 20,000 feet, 210 KIAS. Again, no turbulent wedge appears off the trip. However, spanwise lines are visible throughout the wing surface and chordwise lines appear aft of the boundary layer energizers (BLEs). The light spanwise lines are probably caused by the multiple spars in the Learjet wing that are kept warm by fuel; the fuel is warm as a result of heat absorbed on the ground and at lower altitudes. The chordwise lines are unlikely to be caused by underlying structure or they would appear throughout the wing surface. The lines begin between the BLE elements and are probably the result of

relatively strong flow interaction between the BLEs. The region showing the chordwise lines is in turbulent flow and is not covered by the black, insulative film. There are also fuel tanks within this region of the wing. The fuel tanks extend from spar 1 (just behind the leading edge) to spar 7 (a short distance ahead of the aileron).

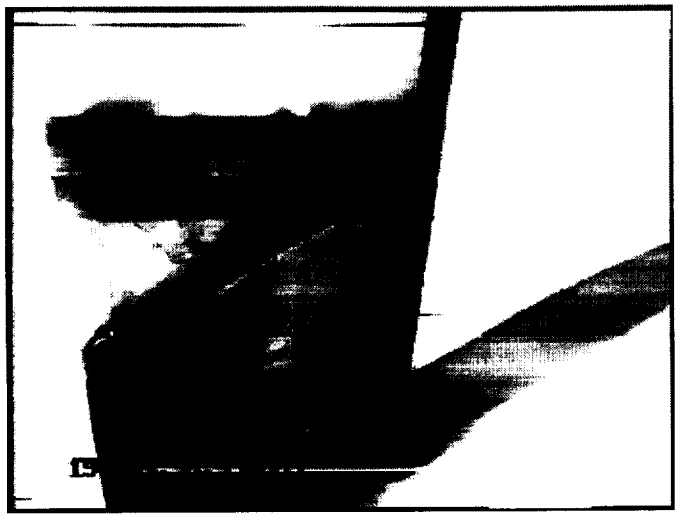

**Figure 8.** Thermogram of the Learjet 24 at 20,000 feet, 210 KIAS. The outboard region of the starboard wing is shown.

### IIIc. Visualization of shocks

The Learjet flights also provided an opportunity to examine the feasibility of shock visualization with in-flight infrared imaging.

As shown in Figure 9, the shock at approximately 55% of chord causes a drop in skin friction coefficient of approximately 0.002. The shock was not visible in the recorded thermograms, but visualization was hindered by the lack of surface treatment and the presence of fuel within the wing at the predicted shock location. Fuel is expected to act as a large thermal mass, smearing and attenuating temperature gradients. In addition, as described above, the BLEs may influence the flow in the region where the shock is expected; shock development and, hence, the skin friction distribution may be affected, making shock detection more difficult.

Numeric simulations were performed with MSES to determine conditions at which shock visualization is most likely. The simulations were set from 40,000 feet to the Learjet 24's service ceiling of 43,000 feet at Mach 0.79 and Mach 0.81. Figure 10 shows the predicted skin friction distributions at 40,000 feet, Mach 0.81 and 30,000 feet, Mach 0.59. Mach 0.81 is within the Learjet's performance capabilities, but the stick puller is activated at this speed, complicating formation flight.

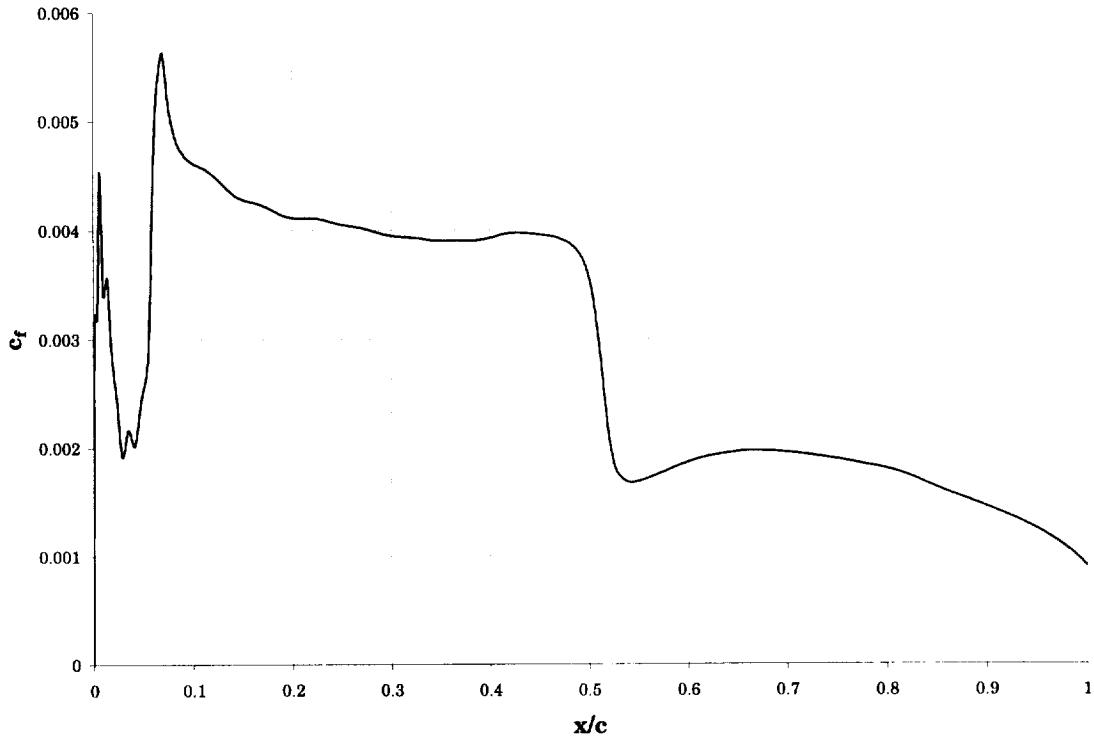


**Figure 9.** Skin friction distribution on the upper surface of the Learjet 24 at 40,000 feet, Mach 0.77. Transition is fixed near the leading edge to simulate the presence of the Softflite kit's leading edge triangles.

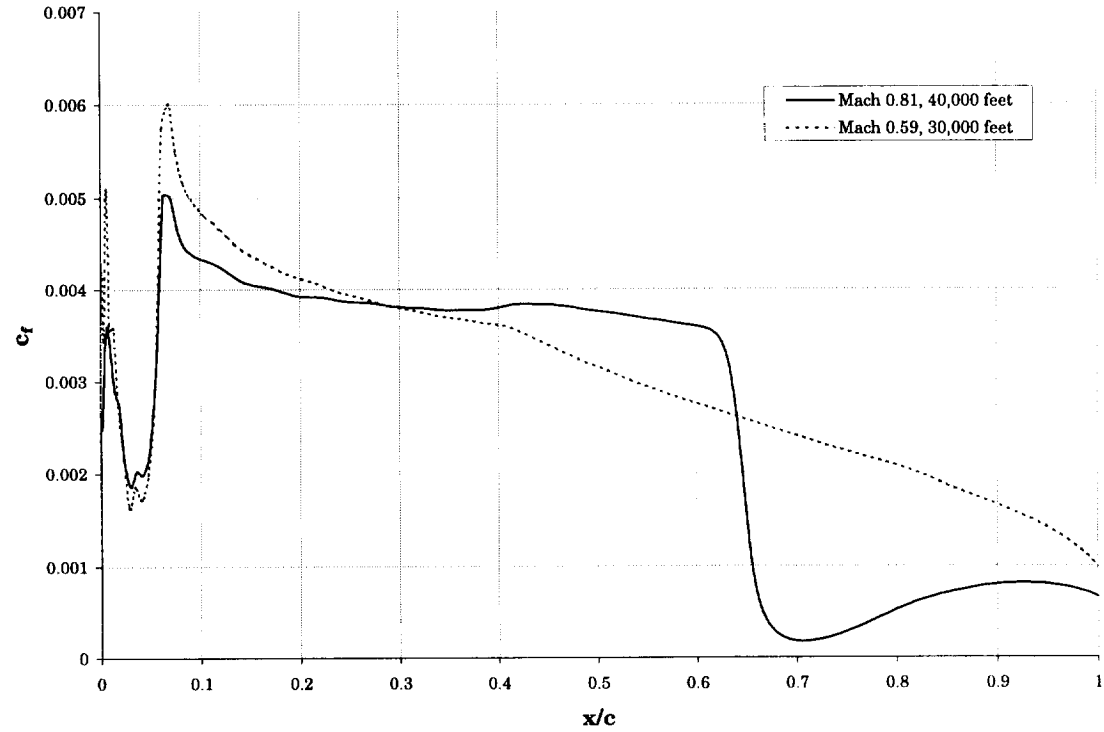


**Figure 10.** Skin friction distribution on the upper surface of the Learjet 24 at 40,000 feet, Mach 0.81 and 30,000 feet, Mach 0.59. Transition is fixed near the leading edge in both cases.

At 30,000 feet, Mach 0.59, no shocks exist and the skin friction distribution is smooth. At Mach 0.81, a shock exists at approximately 65% of chord and a corresponding drop of approximately 0.0033 occurs in the coefficient of skin friction. For comparison, the calculated change in coefficient of skin friction across transition on the T-34C, shown in Figure 3, is 0.0056. Although the skin of the Learjet is thicker than the T-34C, it is expected that the temperature gradient caused by the skin friction drop is large enough to be visualized given appropriate surface treatment.

At altitudes greater than 40,000 feet, the skin friction drop at the shock does not significantly increase. At Mach 0.81 and the Learjet 24's service ceiling of 43,000 feet, the skin friction change increases only 7% to 0.00353. Above 41,000 feet, special oxygen considerations are required for aircrews. Flight experiments investigating shock visualization with the Learjet 24 are therefore recommended at or below 40,000 feet. Note that the flow phenomenon from the BLEs, described above, occurs in the same region where the shock is expected and may affect formation and/or visualization of the shock.

### IIId. Removal of horizontal banding

As stated above, all the thermograms recorded by F/A-18 #846's NITE Hawk exhibit horizontal banding which darken or lighten lines in the image. The banding was characterized and a procedure to remove it was formulated and applied. Although the procedure was not successful, a second, more rigorous method was developed which uses calibration images of established intensity values. With the availability of a new infrared imaging system, implementation of the calibration image procedure was deferred.

*Brief overview of the banding recorded by F/A-18 #846's NITE Hawk*

NASA Dryden's F/A-18 #846 is equipped with an AN/AAS-38 NITE Hawk infrared system. The NITE Hawk records infrared as greyscale video on conventional Hi-8 videotape. In investigations of flow visualization via infrared thermography, video recorded by F/A-18 #846 consistently showed horizontal banding which darkened or lightened lines in the image. The banding detrimentally obscured parts of the subject in the image. A typical image, captured in spring of 1997, is shown in Figure 11.

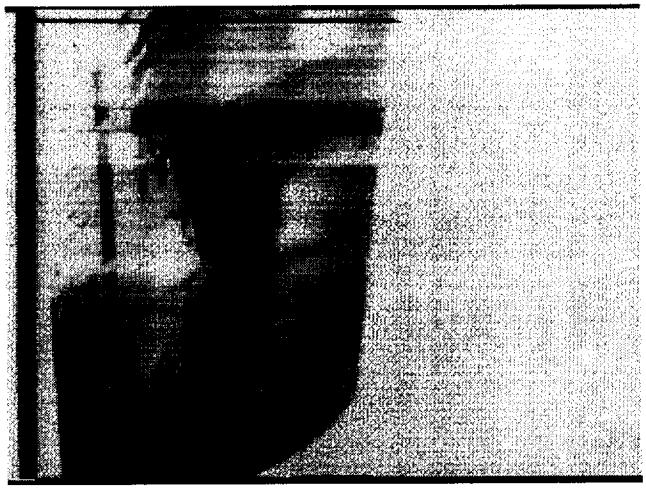

**Figure 11.** An infrared video frame from F/A-18 #846's NITE Hawk. This footage was recorded in spring of 1997.

In fall of 1997, F/A-18 #846 was serviced including maintenance to the NITE Hawk system. As shown in Figure 12, while powered from an external ground source, infrared video did not show the pronounced banding visible in earlier recordings although faint, regular horizontal banding scrolled upward at a steady rate.

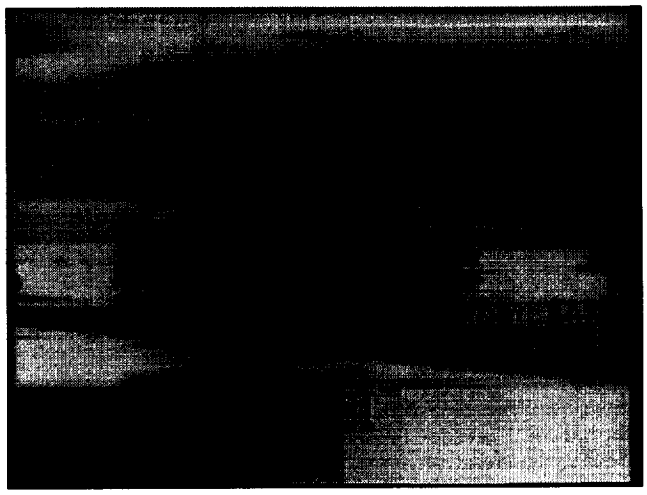

**Figure 12.** An infrared video frame from F/A-18 #846's NITE Hawk after maintenance in fall 1997. The aircraft was powered from an external ground source.

However, video recorded in-flight while systems were internally powered from the engines showed the same banding as in earlier flights.

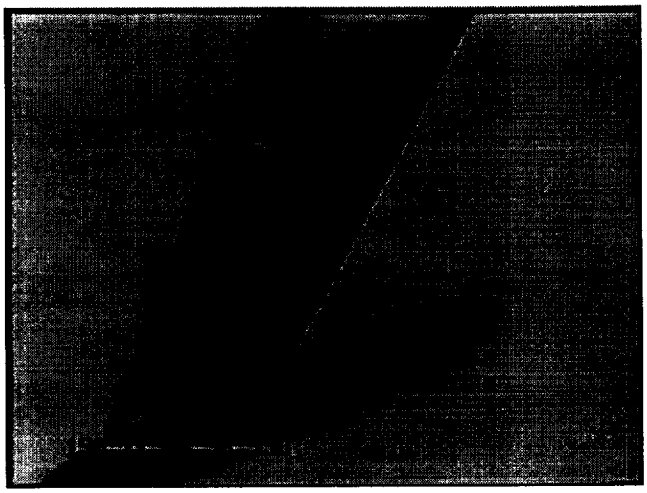

**Figure 13.** An infrared video frame from F/A-18 #846's NITE Hawk while the aircraft was powered internally from its engines. This footage was recorded in July 1998.

The banding, a cursory attempt to remove it, and a more thorough, rigorous removal procedure are discussed below.

*Characteristics of the banding*

Through one flight with a T-34C, one ground test, and two flights with a Learjet 24, the following observations have been made about the banding recorded by F/A-18 #846's NITE Hawk system.

- The banding only occurs when the F/A-18's systems are internally powered by its engines.
- The banding does not appear on the NITE Hawk's control display in the F/A-18's cockpit; however, it is recorded on videotape.
- The infrared imager's resolution is 875 lines, but the video recorder's resolution is only 525 lines. The scan conversion required to record to video likely contributes to the banding.
- The video recorded by the visible spectrum camera collocated in the NITE Hawk's pod does not exhibit any banding.
- On a given line (horizontal row of the video) with banding noise, the nominal intensity is usually changed by a simple positive or negative additive constant.
- The additive constant varies between lines, but usually appears similar (given the same gain and level settings) for a given line throughout all the recorded video, as shown in Figure 13.
- In some image regions, the banding does not appear. This seems to occur where intensities are higher (i.e., closer to white). This is evident in Figure 14 and the backgrounds of the images in Figure 13.
- The magnitude of the banding is dependent on the gain and level settings of the NITE Hawk. This is especially evident in the Learjet footage recorded in July 1998 where level and gain settings were recorded on the audio track.
- The time reading at the lower left is updated more often in the visible spectrum recording than in the infrared recording. The frequency of updating may be related to the video's path from camera to recorder.

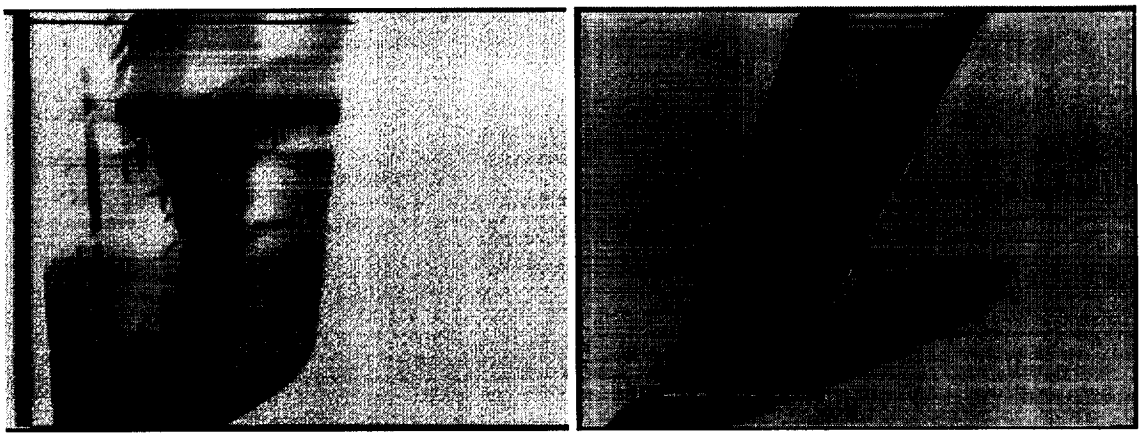

**Figure 14.** These are the same images shown in Figures 11 and 13. They were recorded more than a year apart with maintenance performed on the NITE Hawk in the interim. However, when these images are viewed side-by-side, the location and magnitude of banding show similarities.

*An initial attempt at banding removal*

Ideally, the source of the banding would be identified and eliminated. It is interesting to note that the visible spectrum recorder shows no banding although both recorders are presumably powered by the same source. It has been hypothesized that the noise is

introduced when the video is passed through the F/A-18's system bus. However, this is difficult to verify without more knowledge of the NITE Hawk's internals.

Because information about the F/A-18 and NITE Hawk is limited and modifications are difficult to effect, a post processing, image processing method was developed. This method was cursorily implemented with little success. However, it forms the foundation for a more thorough implementation, detailed later.

The image processing procedure consists of the following:

1. Capture a "calibration image" with the NITE Hawk. The subject of the calibration image is of uniform intensity and fills the entire video frame.
2. Define a "base grey" which is the nominal intensity of the subject.
3. Form a "correction template" by calculating the difference between the base grey and actual intensities in the calibration image.
4. Apply the correction template to an actual frame.

Details of the implementation of the above procedure follows.

The subject of the calibration image was open sky. Initially, no banding was visible as shown in Figure 15. This was consistent with previously recorded images of sky in the background of T-34C and Learjet studies, seen in Figures 11 and 13.

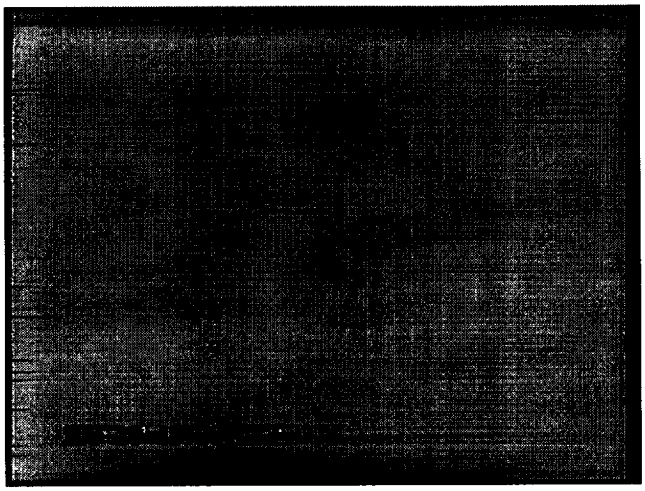

**Figure 15.** A frame from the infrared video footage of open sky recorded for use as a calibration image. Initially, no banding was visible. This footage was recorded on July 9, 1998.

However, during the one minute segment of sky, banding appeared twice when portions of the F/A-18 likely entered the infrared camera's frame. Although the infrared footage does not show any obvious portions of the airplane, the wing and other aircraft parts were recorded by the visible spectrum camera. The location of banding does not seem to directly correlate to how much of the aircraft appeared before the visible spectrum camera.

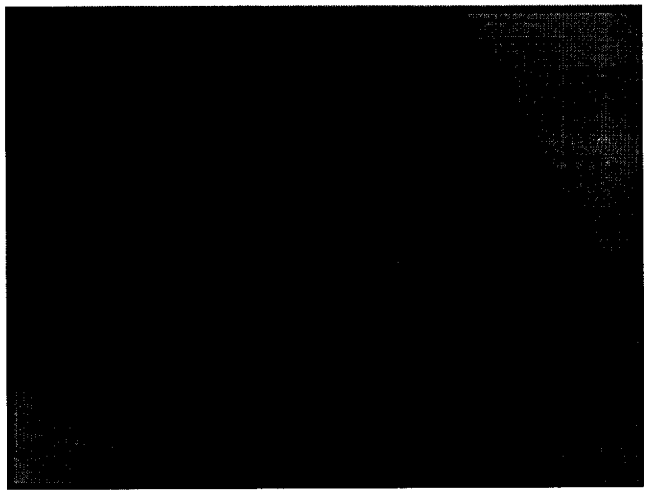

**Figure 16.** Banding appeared for a 3 second and 20 second period during recording of sky. This image is from the first, 3 second segment of banding.

To produce the calibration image, ten frames of the first banded sky segment were averaged. To further suppress non-banding noise, each line was then averaged to produce a column vector of the mean row intensities. The crosshairs at the center of the image and the time reading at the lower left were excluded from the line averages.

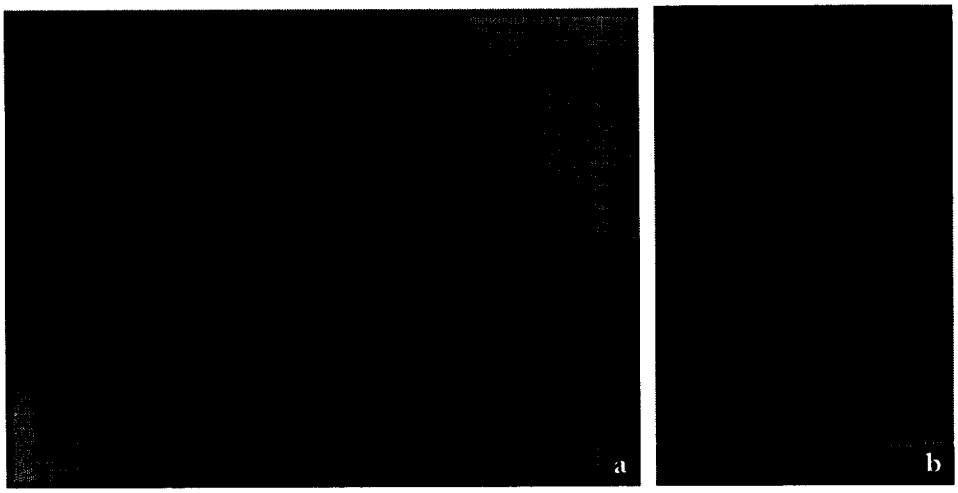


**Figure 17a.** Average of ten frames of the first segment of banded sky. **17b.** Mean row intensities calculated by averaging each line. The image has been widened for clarity.

Figure 18 compares a typical video frame with the mean row intensities. The correlation of banding is not very good, although there are regions with similarities.

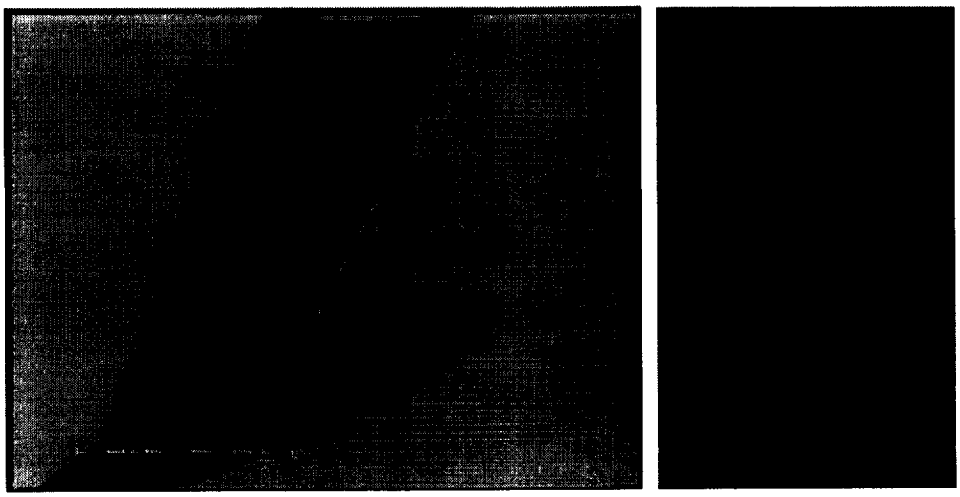

**Figure 18.** The image to the left is the same as in Figure 13. Again, the image of the mean row intensities to the right has been widened for clarity.

The base grey was arbitrarily chosen as 0.30 (0 is black and 1 is white). A "correction column vector" was calculated and applied to a typical frame, shown in Figure 19. The resulting image was not very good.

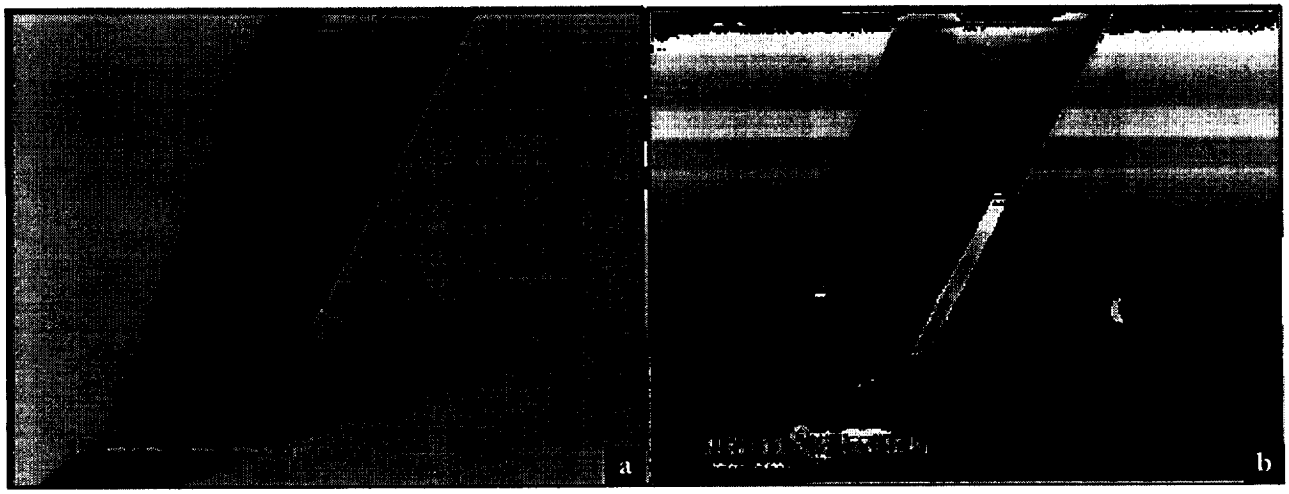


**Figure 19a.** The original image. **19b.** The same image with the correction column vector applied.

Different base grey values were selected with similarly poor results.

In Figure 20, the corrected image is presented again, but with its histogram stretched to optimize the use of available intensities. Note that the selection of the base grey value has no effect on the histogram stretched image.


**Figure 20a.** The original image. **20b.** The same image with the correction column vector applied and its histogram stretched.

*Proposal of a more rigorous method*

In the above implementation, the calibration image did not accurately reflect the banding, as shown in Figure 18. Capturing a more controlled calibration image may yield better results.

A good calibration image might be captured if the following guidelines are observed.

- The recording is performed on the ground. However, power must be from the F/A-18's engines and not an external power source.
- A well defined subject is used. A good subject may be a flat panel filling the camera's frame with three vertical, equally sized regions of the following intensities: black, white, and 18% grey (commonly used for exposure calibration in still photography). Lighting of the subject should be indirect with no glare or reflections.
- The level and gain settings are varied systematically. A different calibration image may be necessary for each level and gain setting. Currently, the level and gain settings are not well understood. Systematic variation of level and gain may also contribute to an overall better understanding of these settings.

### IIIe. Wing surface temperature model

The temperature distribution on a wing in flight was numerically modeled to provide quantitative values for comparison with experimental temperature distributions from thermograms. The numeric solutions also provide a basis for the required temperature range and sensitivity of infrared imagers used in this application.

Assuming a wing section with little taper and sweep, the spanwise temperature gradient is small and a two dimensional model is adequate. The wing section's skin is modeled as a thin wall with uniform temperature throughout its depth at a given chordwise location. The wing skin is discretized into chordwise segments.

The temperature distribution is determined through heat transfer calculations. Heat transfer is governed by the first and second laws of thermodynamics. For this application, the first law can be expressed as:

$$\frac{\partial}{\partial t}\iiint_V \rho c_p T dV = -\iint_A q'' dA \qquad [2]$$

As illustrated in Figure 21, there are four significant sources of heat transfer at each wing segment:

$$\frac{\partial}{\partial t}\iiint_V \rho c_p T dV = -\iint_A (q''_{conv} + q''_{rad} + q''_{sol} + q''_{cond}) dA \qquad [3]$$

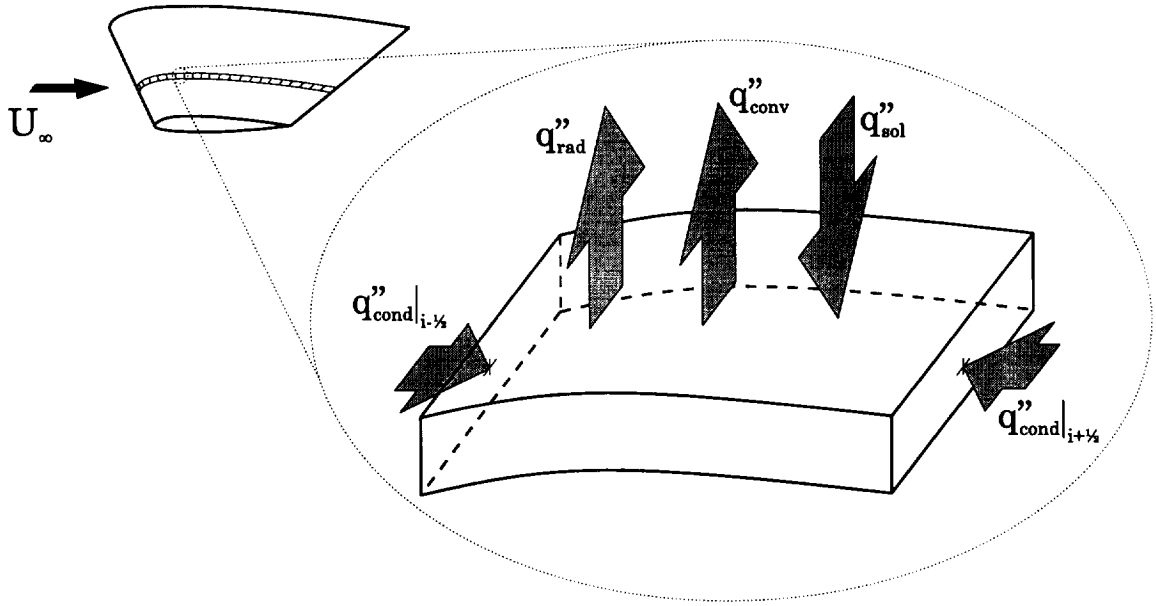


**Figure 21.** Heat transfer mechanisms on a wing in subsonic flight.

$q''_{conv}$ is the convective heat transfer due to flow over the wing. As detailed in Equation 1, the convective heat transfer is dependent on skin friction.

$q''_{rad}$ is the heat transfer due to radiation from the wing surface.

$$q''_{rad} = \varepsilon \sigma T^4 \qquad [4]$$

$\sigma$ is the Stefan-Boltzmann constant, which relates the maximum possible heat flux radiated by a body to the body's surface temperature. $\varepsilon$ is emissivity, a surface property which relates

the maximum possible heat flux to the actual heat flux emitted by a body; it is dependent on factors such as material, surface finish, and surface color. Given emissivity, surface temperature distributions can be deduced from radiation measurements such as those performed with infrared detectors.

$q''_{sol}$ is the heat transfer due to solar heating. Currently, $q''_{sol}$ includes diffuse atmospheric emissions and is estimated as a constant value of 1300 W/m$^2$.

$q''_{cond}$ is chordwise heat conduction within the wing skin. Fourier's law states that:

$$q''_{cond} = -k\nabla T \qquad [5]$$

Currently, the internal surface of the wing skin is assumed to be adiabatic.

Three models were implemented:

- steady state with heat transfer only through the wet surface (i.e., no chordwise conduction, $q''_{cond} = 0$)
- steady state with chordwise conduction within the skin
- time dependent with chordwise conduction within the skin

The steady state models were solved iteratively. The time dependent model was solved using the backward Euler method with a time step determined through a solution accuracy requirement[24].

The following conditions and properties were used in simulating the T-34C flight experiment.

airfoil: NACA 23012
altitude: 10,000 feet
speed: 165 KCAS
$\alpha$: 1°
chord: 5.1 feet
$t_{skin}$: 0.032 inches
$\rho_{skin}$: 2770 kg/m$^3$
$c_{p_{skin}}$: 875 J/kg·K
$\varepsilon_{skin}$: 0.97

Skin friction values were numerically calculated with MSES. Only the upper surface was modeled; the leading and trailing edges were assumed to be adiabatic.

Figure 22 shows the steady state temperature distribution on the T-34C wing at 10,000 feet, 165 KCAS. The results of both the models with and without chordwise heat conduction within the skin are shown. The strong relationship between skin friction and surface temperature is evident. Accounting for chordwise heat conduction within the skin significantly affects the surface temperature solution.

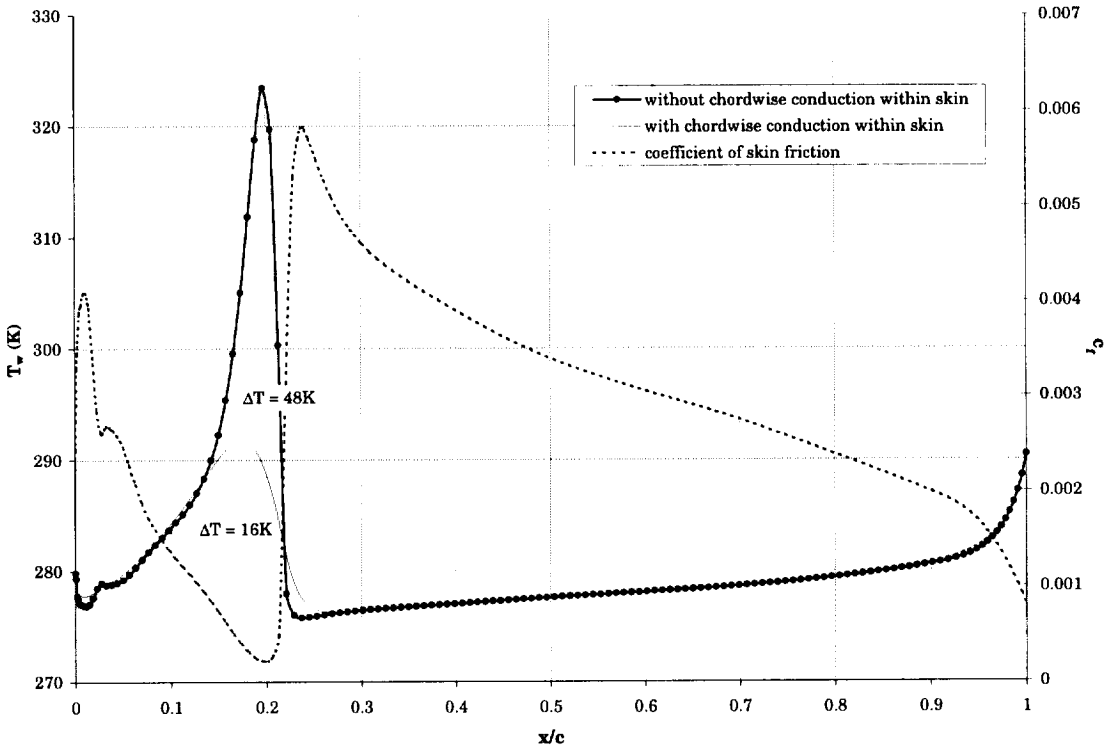


**Figure 22:** Predicted steady state temperature distributions on the T-34C at 10,000 feet, 165 KCAS. The skin friction distribution is also plotted.

When accounting for conduction within the skin, the temperature difference near transition is approximately 15 K, well within the NITE Hawk's thermal resolution. As expected, conduction within the skin smears and reduces the temperature drop induced by transition. The smearing moves the temperature peak forward to 18% of chord.

A corresponding thermogram to the temperature distribution in Figure 22 can be expected to exhibit a visible intensity change somewhere between 19% and 21% of chord. The specific location and appearance of the intensity change cannot be more accurately predicted without quantitative calibration data from the infrared imaging system (e.g., temperatures corresponding to maximum and minimum intensities in the thermogram). Acknowledging this limitation, the thermogram in Figure 3 has good correlation with a large intensity change at 21% of chord. The location of transition was numerically predicted at 21% of chord. Note that because of the smeared temperature drop and the forward shift of the temperature peak, the location of high intensity change and transition do not necessarily coincide.

Figure 23 shows the change over time in surface temperature distribution as the T-34C wing approaches steady state at 10,000 feet, 165 KCAS. The surface starts with the steady state temperature distribution corresponding to sea level flight at Mach 0.3.

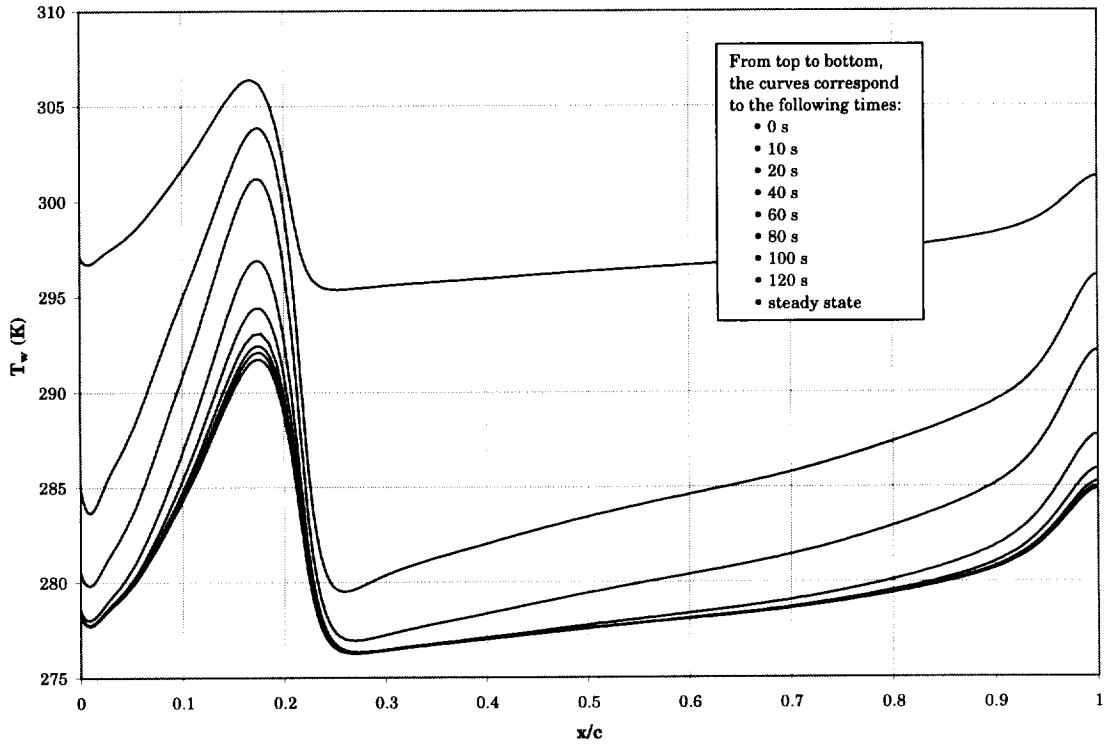


**Figure 23.** History of surface temperature distribution on the T-34C as steady state is approached at 10,000 feet, 165 KCAS. The initial temperature distribution corresponds to steady state at sea level, Mach 0.3.

Assuming an instantaneous climb to 10,000 feet, the wing surface reaches steady state in approximately two minutes. Over this time period, the temperature peak shifts slightly aft from 17% to 18% of chord and the temperature drop reduces from 24 K to 15 K. MSES predicts transition at 20% of chord at sea level and 21% of chord at 10,000 feet.

Currently, the model does not account for changes to the recovery factor due to compressibility. The model can be extended to compressible flow by modifying the $q''_{cond}$ term. $q''_{sol}$, the solar heating term, can also be improved. Direct solar heating and diffuse atmospheric emissions are more accurately modeled as separate terms[25] with solar heating dependent on the orientation of the wing surface relative to the sun's position. Assuming the internal surface of the wing skin to be adiabatic may be inaccurate in some cases, such as when fuel is stored in the wing.

## Conclusions and recommendations

Remote in-flight infrared thermography continues to be a promising technique for flow visualization. This nonintrusive method can be applied to a wide variety of subject aircraft with minimal or no modification necessary on the subject.

Flight experiments investigating visualization of transition at transonic conditions on a Learjet 24 were inconclusive. For more definitive results, it is recommended that future attempts focus on the inboard region of the Learjet's wing where the Softflite kit's leading edge triangles are not installed. The thermograms recorded in the transonic transition visualization experiments were also used for a preliminary study of shock visualization. Shocks were not detected, but nonideal conditions including the lack of surface treatment made successful visualization unlikely. Recommendations of conditions for a future, more detailed study are provided.

Investigations with the current infrared imaging system, an AN/AAS-38 NITE Hawk, are hindered by horizontal banding in the recorded infrared video. The banding limits both qualitative and quantitative analysis of the captured thermograms. An attempt at removing the banding was not successful. Further study of the NITE Hawk's banding was deferred when a new infrared imaging system became available. Alternative infrared systems are briefly reviewed in Appendix I.

A wing surface temperature model was developed to numerically predict surface temperature distributions on a wing in flight. The model provides a theoretical basis for comparison with captured thermograms. The model revealed the significant effect of conduction within the wing skin. Conduction in the skin attenuates temperature gradients and shifts them away from the location of corresponding skin friction changes. Accuracy of the model will be improved by better modeling of atmospheric and solar radiation and incorporation of compressibility effects and internal thermal masses such as fuel.

The introduction of a new infrared imaging system provides opportunities for investigation previously unavailable with the current infrared system. With images unobscured by banding, much more detailed analysis of thermograms will be possible. Further experimentation is required to determine the extent of applicability of the remote in-flight infrared visualization technique.

## References


[1] Holmes, B.J., Obara, C.J., and Yip, L.P. Natural laminar flow experiments on modern airplane surfaces. NASA TP 2256, June 1984.

[2] Quast, A. Detection of transition by infrared image technique. *Proceedings of the ICIASF Record*, Williamsburg, VA, June 22-25, Institute of Electrical and Electronics Engineers, New York, 1987, pp. 125-134.

[3] Hall, R.M., Obara, C.J., Carraway, D.L., Johnson, C.B., Wright, R.E., Jr., Covell, P.F., and Azzazy, M. Comparisons of boundary-layer transition measurement techniques at supersonic Mach numbers. *AIAA Journal*, Vol. 29, No. 6, June 1991, pp. 865-879.

[4] Cattafesta, L.N., III and Moore, J.G. Transition detection in high-speed flows with luminescent temperature-sensitive paint. *Flow Visualization VII*, J. Crowder (ed.), Begell House, pp. 944-949.

[5] Kennelly, R.A., Jr., Westphal, R.V., Mateer, G.G., and Seelen, J. Surface oil film interferometry on a swept wing model in supersonic flow. *Flow Visualization VII*, J. Crowder (ed.), Begell House, pp. 302-307.

[6] Yip, L.P., van Dam, C.P., Whitehead, J.H., Hardin, J.D., Miley, S.J., Potter, R.C., Bertelrud, A., Edge, D.D., and Willard, P.E. The NASA B737-100 high-lift program – measurements and computations. *The Aeronautical Journal*, Vol. 99, No. 989, November 1995, pp. 372-386.

[7] Greff, E. In-flight measurement of static pressures and boundary-layer state with integrated sensors. *Journal of Aircraft*, Vol. 28, No. 5, May 1991, pp. 289-299.

[8] Yip, L.P., Vijgen, P.M.H.W., Hardin, J.D, and van Dam, C.P. In-flight pressure measurements on a subsonic transport high-lift wing section. *Journal of Aircraft*, Vol. 32, No. 3, May-June 1995, pp. 529-538.

[9] Brandon, J.M., Manuel, G.S., Wright, R.E., and Holmes, B.J. In-flight flow visualization using infrared imaging. *Journal of Aircraft*, Vol. 27, July 1990, pp. 612-618.

[10] Swenson, B.L. and Edsinger, L.E. Preliminary analysis of remote infrared imagery of shuttle during entry – an aerothermodynamic flight experiment. NASA TM 73251, Oct. 1977.

[11] O'Lone, R.G. NASA experimenters studying data on reentry heating of orbiter Columbia. *Aviation Week & Space Technology*, April 12, 1982, pp. 68-71.

[12] Green, M.J., Budnik, M.P., Yang, L., and Chiasson, M.P. Supporting flight-data analysis for space-shuttle orbiter experiments at NASA Ames Research Center. NASA TM 84345, April 1983.

[13] Horstmann, K.H., Redeker, G., Quast, A., Dreßler, U., and Bieler, H. Flight tests with a natural laminar flow glove on a transport aircraft. AIAA Paper 90-3044-CP, 1990.

[14] Van Dam, C.P., Shiu, H.J., and Banks, D.W. In-Flight Flow Visualization Using Infrared Thermography. NASA CR-97-207087, November 1997.

[15] Van Dam, C.P., Shiu H.J., and Banks, D.W. Remote In-Flight Boundary Layer Transition Visualization using Infrared Thermography. Paper 181, *CDROM Proceedings of 8th International Symposium on Flow Visualization*, G.M. Carlomagno and I. Grant (eds.), Sorrento, Italy, September 1998.

[16] Brinkman, D. (ed.). *Jane's Avionics 1991-92.* Jane's Information Group, Sentinel House, UK, 1991.

[17] Rogers, S.E. and Kwak, D. An Upwind Differencing Scheme for the Steady-State Incompressible Navier-Stokes Equations. *Journal of Applied Numerical Mathematics*, Vol. 8, 1991, pp. 43-64.
[18] Rogers, S.E., Wiltberger, N.L., and Kwak, D. Efficient Simulation of Incompressible Viscous Flow over Single and Multielement Airfoils. *Journal of Aircraft*, Vol. 30, No. 5, Sept.-Oct. 1993, pp. 736-743.
[19] Drela, M. Newton solution of coupled viscous/inviscid multielement airfoil flows. AIAA Paper 90-1470, June 1990.
[20] Angelucci, E. *World Encyclopedia of Civil Aircraft; From Leonardo Da Vinci to the Present.* Crown Publishers, Inc., New York, 1982.
[21] Taylor, J.W.R. (ed.). *Jane's All The World's Aircraft 1987-88.* Jane's Publishing Company Limited, England, 1987.
[22] Szurovy, G. *Learjets.* Motorbooks International Publishers & Wholesalers, USA, 1996.
[23] Hinson, M.L. Devices for Improvement of Controllability at Stall. SAE Paper 830723, 1983.
[24] Dwyer, H.A., Yam, C., Tang, K., and McKillop, A. *Computational Methods in Heat Transfer; Notes for ME165.* Department of Mechanical Engineering, University of California, Davis, Davis, California, Fall 1994, pp.37-39.
[25] Incropera, F.P. and DeWitt, D. *Introduction to Heat Transfer.* Courier Companies, Inc., USA, 1990.

## Appendix I. Commercially available infrared imaging flight systems

Commercially available infrared cameras that can be used for in-flight boundary layer visualization were investigated.

Infrared imaging is commonly used in military, surveillance, and industrial inspection applications. These cameras can be adapted for flow visualization. The function, applicability, and pertinent specifications of infrared cameras are well described by Kaplan[i].

The requisite spectral sensitivity can be determined by Wien's Displacement Law and estimates of the temperatures that will be measured. Wien's Displacement Law is presented below; T, the temperature, is expressed in units of Kelvin (K) and $\lambda_p$, the peak emitted wavelength, is in micrometers (μm).

$$\lambda_p = \frac{2897.8}{T} \qquad [I.1]$$

The table below tabulates altitude, ambient air temperature given a standard atmosphere, and equivalent emitted peak wavelength. Actual encounter temperatures tend to be higher due to absorption of solar radiation, atmospheric emissions, and flow compressibility effects.

| altitude (ft) | T (°C) | $\lambda_p$ (μm) |
|---|---|---|
| 0 | 15.0 | 10.05 |
| 10000 | -4.8 | 10.80 |
| 20000 | -24.6 | 11.66 |
| 30000 | -44.3 | 12.66 |

Emissions can therefore be expected to be in the 8 to 13 μm range. This coincides with the range commonly known as long wave infrared (LWIR). Long wave IR is generally described as 8 to 12 μm, corresponding to -32°C to 89°C.

Long wave infrared cameras tend to be expensive because of their high sensitivity. Recent indium-antimonide (InSb) medium wave infrared (MWIR) may provide a more economical solution. InSb cameras are most effective in the medium wave range, but they remain sufficiently sensitive at the longer wavelengths associated with flow visualization applications.

A table of some commercially available long wave and InSb medium wave infrared cameras, performance specifications, and approximate cost is presented on the following page. The Lockheed Martin NITE Hawk, listed first, is not commercially available. However, it is the camera currently in use and is provided as a benchmark for comparison.

In addition to Kaplan's performance parameters, a camera for in-flight applications must be readily mountable on aircraft. Handheld and stationary cameras are also detailed in the following table. These cameras can be adapted to airborne applications via third party products. Both Mitsubishi and Inframetrics representatives have referred to Versatron as a supplier of gimbals and aircraft mounts.

Of the systems documented, the FLIR SAFIRE, FLIR Star SAFIRE, FLIR UltraPower-570, FLIR Ultra 6000, FLIR Ultra 4000, and Inframetrics 445G-MKII meet the spectral sensitivity requirements and are ready for aircraft mounting "out of the box". The

---

[i] Kaplan, Herbert. Commercial applications for thermal imaging instruments, an update. *SPIE - The International Society for Optical Engineering*, Vol. 2269, July 1994, pp.8-17.

Mitsubishi IR-G600 can detect only shortwave IR and, while designed specifically for installation in a gimbal, does not include a gimbal.

The 445G-MKII is incapable of recording quantitative data. There is therefore no internal method for correlating intensity values with temperatures when viewing recorded thermograms. The SAFIRE does not have this shortcoming and includes a laser range finder and digital autotracker. However, the SAFIRE, at $290,000, is almost two and a half times as much in cost. The Ultra 4000 is essentially the SAFIRE integrated with a visible spectrum camera; the Ultra 4000 is therefore likely to be more expensive than the SAFIRE. The relatively new UltraPower-570 is inexpensive, but little information is currently known about this system. The Star SAFIRE and Ultra 6000 are indium-antimonide medium wave cameras and may be an economical solution; again, little information is currently known about these systems. Specifications and details on the UltraPower-570, Star SAFIRE, Ultra 6000, and any other systems will be forwarded as they are received.

As stated above, an alternative solution may be a third party gimbal paired with a handheld camera such as the Inframetrics 760 or the Raytheon Radiance indium-antimonide systems. The 760 and Radiance are established cameras with a wide range of available optics and facility for direct digital acquisition. The gimbal could also be used with other cameras for different applications. Although gimbals are expensive, it is likely that the combined cost of a gimbal and a good handheld camera would still fall somewhere between the cost of a 445G-MKII and SAFIRE.

| Manufacturer | Model | Published range (μm, °C, or °F) | Thermal resolution (°C or °F) | Image resolution (pixels) | Picture FOV | Gimbal? | Estimated cost | Notes |
|---|---|---|---|---|---|---|---|---|
| Lockheed Martin | NITE Hawk | 8-12 μm | < 0.1°F | | 3°×3°, 12°×12° | y | | |
| FLIR, Inc. | SAFIRE™(AN/AAQ-22) | 3-5 μm or 8-12 μm | | | 5°×3°, 28°×16.8° | y | $290,000 | Merged with Agema; includes range finder, digital autotracker; long wave is scanned, not focal plane array. |
| FLIR, Inc. | Star SAFIRE | 3-5 μm | | | 3 fields of view available in standard configuration | y | | InSb; optional visible spectrum camera, autotracker, and video recorders; complies with military specifications. |
| FLIR, Inc. | UltraPower-570 | longwave | < 0.1°C | 320×240 | 12° | y | ≈$100,000 | Microbolometer focal plane array; includes visible spectrum camera. |
| FLIR, Inc. | Ultra 6000 | medium wave | | 256×256 | 4°, 20° | y | | InSb; includes visible spectrum camera; optional autotracker. |
| FLIR, Inc. | Ultra 4000 | 8-12 μm | | | 5°×3°, 28°×16.8° | y | | Same infrared imager as SAFIRE but includes visible spectrum camera. |
| FLIR, Inc. | Agema 570 | 7.5-13 μm | 2°C | 320×240 | 24° | n, handheld | ≈$50000; +$10000 for TRACER | Can be interfaced with TRACER for direct digital acquisition. |
| FLIR, Inc. | Agema 510 | 3-5 μm | 0.1°C at 30°C | 320×240 | | n, handheld | $12950 | |
| FLIR, Inc. | SeekIR | 8-14 μm | 0.1°C at 30°C | 320×240 | | n, handheld | $12950 | |
| Inframetrics | 445G-MKII | 8-12 μm | <0.1°C | 445 lines | 7°, 28° | y | $120,000 | Qualitative information only, no quantitative data recorded; includes visible-spectrum CCD camera. |
| Inframetrics | Model 760 | 3-12 μm or 8-12 μm | <0.1°C | | 20° h ×15° v, other optics available | n, handheld | $60000; available used for ≈$42000; +$12000 for ThermaGRAM (not including computer) | Built-in direct digital output to floppy disk or PC with Thermagram. |

| Manufacturer | Model | Published range (μm, °C, or °F) | Thermal resolution (°C or °F) | Image resolution (pixels) | Picture FOV | Gimbal? | Estimated cost | Notes |
|---|---|---|---|---|---|---|---|---|
| Inframetrics | Model 740 | 8-12 μm | <0.1°C | | 20° h ×15° v, other optics available | n, handheld | $48,000 | No direct digital out; can be upgraded to Model 760. |
| Raytheon | Radiance HS LW | longwave | .003K to .004K | 256×256 | | n | $150,000 | Merged with Amber, TI, & Hughes IR divisions; direct digital output via ImageDesk. |
| Raytheon | Radiance HS | 3-5 μm | | 256×256 | variety of optics available | n | $90000; $100000 with ImageDesk | InSb; direct digital output via ImageDesk. |
| Raytheon | Radiance 1 | 3-5 μm | | 640×482 | | n | $60000; $75000 with ImageDesk | InSb; less sensitive and less rugged than Radiance HS; direct digital output via ImageDesk. |
| Raytheon | PalmIR-250 | 7-14 μm | 0.5°C | 320×240 | 12° × 9° | n, handheld | $13,000 | |
| Raytheon | ExplorIR | -20 to +300 °C or -20 to +900 °C | 0.15°C | 320×236 | | n, handheld | | |
| Raytheon | Sentinel | 8-12 μm | | 320×240 | 13.7° × 18.3° | n, handheld | | |
| Raytheon | 1000 series | 7.5-13.5 μm | | | 40° h × 30° v, 15° h × 11.25° v, or 9° h × 6.75° v | n, stationary or handheld | | Primarily for security applications. |
| Raytheon | NIGHTSIGHT 200W | longwave (8-14 μm) | | 320×164 | 12° × 6° | n, car mount | $10,000 | With pan-tilt head; primarily for security applications. |
| Mitsubishi | IR-G600 | optimally 3-5 μm, up to 1-6 μm | 0.08°C at 25°C | 512×512 | | y, not included | $72000, gimbal not included | |